Evidence for a quantum-spin-Hall phase in graphene decorated with Bi_2Te_3 nanoparticles

K. Hatsuda[1], H. Mine[1], T. Nakamura[2], J. Li[3], R. Wu[3], J. Alicea[4], S. Katsumoto[2], J. Haruyama[1,2*]

[1]*Faculty of Science and Engineering, Aoyama Gakuin University, 5-10-1 Fuchinobe, Sagamihara, Kanagawa 252-5258, Japan*

[2]*Institute for Solid State Physics, The University of Tokyo, 5-1-5 Kashiwanoha, Kashiwa, Chiba 277-8581,* Japan

[3]*Department of Physics and Astronomy, University of California, Irvine CA 92697-4575, USA*

[4]*Department of Physics, Institute for Quantum Information and Matter, and Walter Burke Institute for Theoretical Physics, California Institute of Technology, Pasadena, CA 91125, USA*

[*]To whom correspondence should be addressed. E-mail: J-haru@ee.aoyama.ac.jp

Realization of the quantum-spin-Hall effect in graphene devices has remained an outstanding challenge dating back to the inception of the field of topological insulators. Graphene's exceptionally weak spin-orbit coupling—stemming from carbon's low mass—poses the primary obstacle. We experimentally and theoretically study artificially enhanced spin-orbit coupling in graphene via random decoration with dilute Bi_2Te_3 nanoparticles. Remarkably, multi-terminal resistance measurements suggest the presence of helical edge states characteristic of a quantum-spin-Hall phase; those magnetic-field dependence, X-ray photoelectron spectra, scanning tunneling spectroscopy, and first-principles calculations further support this scenario. These observations highlight a pathway to spintronics and quantum-information applications in graphene-based quantum-spin-Hall platforms.

Graphene played a key historical role in the development of topological insulators (*1*,*2*)—materials that exhibit an electrically inert interior yet form exotic metals at their boundary. In 2005, Kane and Mele predicted that coupling between the spin and orbital motion of electrons turns graphene into a 'quantum-spin-Hall (QSH)' insulator that hosts spin-filtered metallic edge states with inherent resilience from scattering (*3*). These novel edge states underlie tantalizing technological applications for low-power electronics, spintronics devices, and fault-tolerant quantum computing (*4-6*). Although graphene's intrinsic spin-orbit coupling is far too weak to produce an observable QSH phase in practice, numerous alternative platforms were subsequently discovered, including HgTe (*7-10*) and InAs/GaSb quantum wells (*11*,*12*), WTe_2 (*13-15*), bismuthene (*16*), and the layered compound $Bi_{14}Rh_3I_9$ (*17*,*18*).

Ease of fabrication, measurement, and manipulation of graphene nevertheless continues to strongly motivate efforts at fulfilling Kane and Mele's original vision. Might it be possible to externally boost graphene's spin-orbit coupling to stabilize a robust QSH phase, in turn opening an appealing pathway towards applications? Numerous theory works have pursued this line of attack via introduction of foreign atoms or via substrate engineering (*19-22*); these methods have been predicted to elevate the bulk band gap for the QSH phase by several orders of magnitude compared to that in pure graphene. Implementation of these proposals has, however, so far proven challenging despite recent efforts (*23-26*).

Here we present the first experimental evidence for the formation of an 'engineered' QSH phase in a graphene device. Specifically, we explore graphene decorated with dilute, randomly positioned

Bi_2Te_3 nanoparticles. These nanoparticles carry giant spin-orbit coupling via. tunneling current and can thus significantly modify graphene's electronic structure even at very low coverages (*26*); they can also be inserted into the graphene lattice in a minimally invasive way. Most strikingly, we perform non-local resistance measurements on multiple devices and find *quantitative* agreement with the response expected from dissipationless edge-state conduction in a QSH phase. Those perpendicular magnetic-field dependence, scanning tunneling spectroscopy (STS), and first-principles simulations further corroborate this picture. Our results re-establish graphene as an experimentally promising QSH medium and spotlight many avenues of future exploration.

In the present experiments, monolayer graphene is grown by chemical vapor deposition on a SiO_2/Si substrate (area ~1cm^2) and formed into Hall-bar patterns by argon-gas etching with six or four branches to Ti/Au electrode terminals; see Figs. 1A-D and Fig. S1 from Supplementary Material 1 (SM1). Similar multi-terminal devices have been used to detect helical edge states in HgTe quantum wells (*8*). High quality of the monolayer graphene (i.e., low amounts of defects and contamination) is confirmed by Raman spectroscopy and X-ray photoelectron spectroscopy (XPS).

We further deposit Bi_2Te_3 nanoparticles with diameters of ~1-30 nm (Sigma Aldrich Inc.) onto the graphene surface following our previous nanoneedle method (*26*). Specifically, we repeatedly drop and then absorb a small acetone droplet containing the nanoparticles using the narrow tip of the needle (Saito Medical Instruments Inc.), which has an inner-pore diameter of ~50 μm, allowing precise control of the low nanoparticle density D within the graphene Hall bar (SM2 and video). Figure 1E presents an atomic-force-microscope image of a decorated sample with $D \sim 4/100^2$ nm^2 (~3% coverage ratio), which we used for the present experiments. XPS spectra of the samples, Figs. 1F-H, demonstrate a C*1s* orbital peak (~282 eV) arising from Bi-C coupling (Fig. 1F) and a Te$3d_{5/2}$ orbital peak (~574 eV) arising from Te-C coupling (Fig. 1H). These peaks suggest clean, low-damage decoration with Bi_2Te_3 nanoparticles, and also indicate the hybridization required for enhancing graphene's spin-orbit coupling.

Figure 2 presents four-probe resistance measurements obtained in the six- and four-terminal (branch) devices from Figs. 1A and 1C. Current I_{ij} flows from lead i to lead j and the voltage V_{kl} is measured across contacts k and l, yielding a resistance $R_{ij,kl} = V_{kl}/I_{ij}$ that we monitor as a function of back-gate voltage V_{bg}. In a QSH phase, conduction is mediated by helical edge states that equilibrate at the contacts but are otherwise protected from elastic backscattering by time-reversal symmetry. Landauer-Buttiker formalism (*9*) then predicts $R_{ij,kl}$ values quantized to rational fractions of the resistance quantum $R_Q = h/e^2$, where h is Planck's constant and e is the electron charge. Quantized non-local resistances have indeed been previously reported in HgTe quantum wells as evidence for dissipationless helical edge transport (*9*). Figure 2A illustrates $R_{16,34}$ measured for undecorated graphene and with Bi_2Te_3 nanoparticles at coverage ~3%. As expected, without nanoparticles $R_{16,34}$ (measured at room temperature) essentially vanishes for all V_{bg}. Nanoparticle decoration, by contrast, yields an appreciable non-local resistance $R_{16,34}$ even at room temperature. Most interestingly, upon cooling down to T = 1.5 K we find an extended V_{bg} window for which a maximum of $R_{16,34} \approx R_Q/6$ appears—in quantitative agreement with the value expected from helical-edge transport.

All other panels in Fig. 2 correspond to measurements on Bi_2Te_3-decorated graphene at T = 1.5 K. Figure 2B plots $R_{13,46}$, which peaks at ~$2R_Q/3$, while Fig. 2C shows $R_{14,23}$, which peaks at ~$R_Q/2$. (The pronounced minimum in $R_{14,23}$ at V_{bg} ~10V possibly arises from a leakage current between the electrode pad 1 and back gate electrode through *p*-type silicon substrate). Figure 2D presents $R_{14,23}$ for a four-terminal *H*-shaped device at coverage ~3%; this non-local resistance peaks at ~$R_Q/4$. The peak values in Figs. 2B through 2D also agree quantitatively with the helical-edge-state picture. However, the observed $R_{45,13}$ from our six-terminal device (Fig. 2E) significantly overshoots the resistance $R_Q/3$

expected from helical edge states. The origin of this discrepancy is presently unclear. We also detected nonlocal resistances in four other devices (not shown) that significantly undershoot the predicted quantized values—possibly indicating shorting of the current through the bulk of these samples.

Figure 3A illustrates examples of STS measurements on the decorated-graphene devices. No energy gaps are observed with V_{bg}, away from the resistance peaks in Fig. 2. Adjusting the V_{bg} (e.g., 15V) to those coincident with resistance peaks in Fig. 2 yields qualitatively different behavior. For two spectra taken near to two different nanoparticles existing at bulk, clear spectral gaps are visible, ranging in magnitude from ~5-20 meV. This variation is consistent with simulations as explained later (Fig. 4 and SM3), which revel non-uniformity of these gaps as arising from variations in the nanoparticle size, chemical condition (*e.g*., stoichiometry), and their chemical bonding with graphene Dirac states. By contrast, data taken at an edge point shows disappearance of such gaps. Note that these 'V-shaped' like edge spectra qualitatively resemble STS measurements in several other QSH candidates (*14,16,18*). Collectively, our STS experiments further support the emergence of an insulating bulk with gapless helical edge states driven by nanoparticle decoration.

Figure 3B shows low out-of-plane magnetic field ($B_\perp$) dependence of conductance (G), corresponding to inverse of the R peak values of Figs. 2A (blue symbol) and 2D (red symbol) and two off-peak R values (green and pink symbols). The G values for the two R peaks rapidly decrease with increasing $B_\perp$, whereas the G for the off-peal R values decreases just slightly. These behaviors are in qualitatively good agreement with a QSH phase observed in monolayer WTe_2 (*15*) and support that the two R peaks of Figs. 2A and 2D are attributed to the helical edge spins. A QSH phase emerges with a bulk energy gap but gapless helical edge states protected by time-reversal symmetry, in which opposite spin states form a Kramers doublet counterpropagate. Only when a Fermi level is set to Kramers point, R values (G values in Fig. 3B) can well reflect the band gap opening due to Zeeman effect caused by applied $B_\perp$, resulting in the observed decrease in the G corresponding to the two R peaks. The applied low $B_\perp$ gives no influence to the Bi_2Te_3 nanoparticles and tunneling current, because almost no magnetization is observed in magnetization curve of graphene decorated with Bi_2Te_3 nanoparticle in coverage as large as ~10% on $B_\perp$ (Fig. 3C). Thus, the observed G behaviors are determined only by a QSH phase in the graphene.

To explain these experimental findings, we performed density functional theory (DFT) calculations using a large 7×7 graphene supercell containing a Bi_2Te_3 nanoparticle with 10 Bi and 15 Te atoms (the diameter of this cluster is about 1.2 nm). Since the atomic structure of the nanoparticle is unknown, we performed ab initio molecular dynamics (AIMD) simulations by baking it at 600K for 6 picoseconds and then cooling it down to 300 K in 5 picoseconds. The structures obtained through AIMD simulations were further relaxed at 0 K, with the inclusion of the van der Waals correction in DFT calculations. Figures 4A and 4B show side and top views of the optimized structure of the Bi_2Te_3 nanoparticle on graphene. The separation between the nanoparticle and graphene is about 3.4 Å, indicating weak interaction between them—contrary to single Bi atoms, which hybridize strongly with graphene. Moreover, a small corrugation appears in the graphene layer. From the charge-density difference ($\Delta\rho=\rho_{BT/Gr}-\rho_{BT}-\rho_{Gr}$), we see that Bi atoms donate electrons to graphene whereas Te atoms gain electrons from graphene.

Due to the weak van der Waals interaction, the composite system's band structure continues to exhibit Dirac cones (Fig. 4C). Electronic states of the Bi_2Te_3 nanoparticle reside rather far from the Fermi level and disperse weakly, indicating adequacy of the 7×7 supercell for minimizing direct interaction among adjacent nanoparticles. Significantly, the Bi_2Te_3 nanoparticles nevertheless yield a sizeable band gap $E_g \approx 6$ meV at the Dirac point, which sits slightly away from the Fermi level due to the aforementioned charge transfer (Fig. 4D). To determine if the band gap is topologically nontrivial,

we calculated the n-fields and Z_2 invariant from the Bloch functions (*27*,*28*) (Fig. 4E). By counting the positive and negative n-field numbers over the half of the torus—see Fig. 4E—one obtains a nontrivial Z_2 invariant. Test calculations with different k-point meshes consistently reproduce this result. Therefore, DFT predicts that Bi_2Te_3-nanoparticle-decorated graphene realizes a QSH phase, supporting our experimental observations.

To establish robustness of the topological state, we calculated the band structures and Z_2 invariants using an 8×8 supercell with Bi_2Te_3 nanoparticles containing an additional Bi or Te atom. The altered chemical stoichiometry of the nanoparticles shifts the Fermi level as shown in Fig. S3 (SM3). Furthermore, the reduction of Bi_2Te_3 coverage in the 8×8 supercell produces a band gap that is reduced (Fig. S2) yet remains topologically nontrivial in both cases. The band-gap magnitude and Fermi-level position thus appear to be tunable by adjusting the size, coverage, and stoichiometry of Bi_2Te_3 nanoparticles. These features are consistent with STS observations, which demonstrated non-uniform gaps depending on nanoparticles (Fig. 2F), and are clearly attractive for the development of graphene-based QSH devices.

In conclusion, multi-terminal *R* measurements, those magnetic-field dependence, XPS, STS, and first-principles calculations provided strong evidence that helical edge states characteristic of a QSH phase emerge upon random decoration of dilute Bi_2Te_3 nanoparticles (as small as ~3%) into graphene via our nanoneedle method. On the contrary, edge states can arise even in topologically trivial systems (*29*-*31*), *e.g*., due to band bending (*30*) and edge defects (*31*) as observed recently in ordinary graphene near the Dirac point. Although quantized edge resistances were not reported in those graphene studies, it may be important to ask whether our experiments are compatible with such a trivial scenario. Systematically exploring the effects of nanoparticle positions, sizes, and stoichiometry would help further clarification of the present QSH phase. It is highly expected that such experiments will introduce robust QSH phase to the present graphene and open the doors to innovative spintronic devices and quantum-information applications in graphene-based QSH platforms.

References and Notes

1. M. Z. Hasan and C. L. Kane, *Rev. Mod. Phys*. **82**, 3045 (2010).
2. X.-L. Qi and S.-C. Zhang, *Rev. Mod. Phys*. **83**, 1057 (2011).
3. C.L. Kane & E. J. Mele, *Phys. Rev. Lett.* **95**, 226801 (2005).
4. L. Fu and C. L. Kane, *Phys. Rev. B* **79**, 161408(R) (2009).
5. A. Yu. Kitaev, *Annals of Physics* **303**, 2 (2003).
6. C. Nayak *et al., Rev. Mod. Phys*. **80**, 1083 (2008).
7. B. A. Bernevig *et al., Science* **314**, 1757 (2006).
8. M. Konig *et al., Science* **318**, 766 (2007)
9. A. Roth *et al., Science* **325**, 294 (2009).
10. C. Brune *et al., Nature Phys*. **8**, 485 (2012).
11. L. J. Du *et al., Phys. Rev. Lett.* **114**, 096802 (2015).
12. C. Liu et al., *Phys. Rev. Lett.* **100**, 236601 (2008).
13. X. Qian et al., *Science* **346**, 1344 (2014).
14. S. Tan et *al., Nat. Phys*. **13**, 683 (2017).
15. S. Wu et al., *Science* **359**, 76 (2018).
16. F. Reis *et al., Science* **357**, 287 (2017).
17. B. Rasche *et al., Nature Mat.* **12**, 422 (2013).
18. C. Pauly *et al.*, *Nature Phys.* **11**, 338 (2015).
19. C. Weeks *et al., Phys. Rev. X* **1**, 021001 (2011).
20. J. Hu *et al., Phys. Rev. Lett.* **109**, 266801 (2012).
21. H. Jiang *et al., Phys. Rev. Lett.* **109**, 116803(2012).
22. Y. Ren et al., *Rep. Prog. Phys.* **79,** 066501 (2016)
23. Z. Jia *et al., Phys. Rev. B* **91**, 085411 (2015).
24. U. Chandni *et al., Phys. Rev. B* **91**, 245402 (2015).
25. Y. Wang *et al., Scientific Report* **5**, 15764 (2015).
26. T. Nanba, J. Haruyama *et al., Appl. Phys. Lett.* In press http://www.ee.aoyama.ac.jp/haru-lab/
27. T. Fukui & Y. Hatsugai, *J. Phys. Soc. Jpn.* **76**, 053702 (2007).
28. D. Xiao *et al., Phys. Rev. Lett.* **105**, 096404 (2010).
29. F. Nichele *et al., New J. Phys*. **18**, 083005 (2016).
30. M. T. Allen *et al., Nature Phys*. **12**, 128 (2016).
31. M. J. Zhu *et al., Nature Commun*. **8**, 14552 (2017).

Acknowledgements

JH thank Y. Shimazaki, T. Yamamoto, S. Tarucha, T. Ando, S. Tang, Z-X. Shen, M. Dresselhaus, J. Shi, P. Jarillo-Herrero, A. H. Macdonald, and P. Kim for their technical contributions, fruitful discussions, and encouragement. JA also acknowledges J. Eisenstein, M.-F. Tu, and A. Yacoby for illuminating conversations. The work at the Aoyama Gakuin University was partly supported by a grant for private universities and a Grant-in-Aid for Scientific Research (15K13277) awarded by MEXT. Work at the University of Tokyo was partly supported by Grant-in-Aid for Scientific Research (Grant No.26103003). DFT calculations at UCI were supported by DOE-BES (grant no. DE-FG02-05ER46237) and the computer simulations were supported by the National Energy Research Scientific Computing Center (NERSC). Work at Caltech was partially supported by the National Science Foundation through grant DMR-1723367 and the Army Research Office under Grant Award W911NF-17-1-0323; the Institute for Quantum Information and Matter, an NSF Physics Frontiers Center with support of the Gordon and Betty Moore Foundation through Grant GBMF1250; and the Walter Burke Institute for Theoretical Physics.

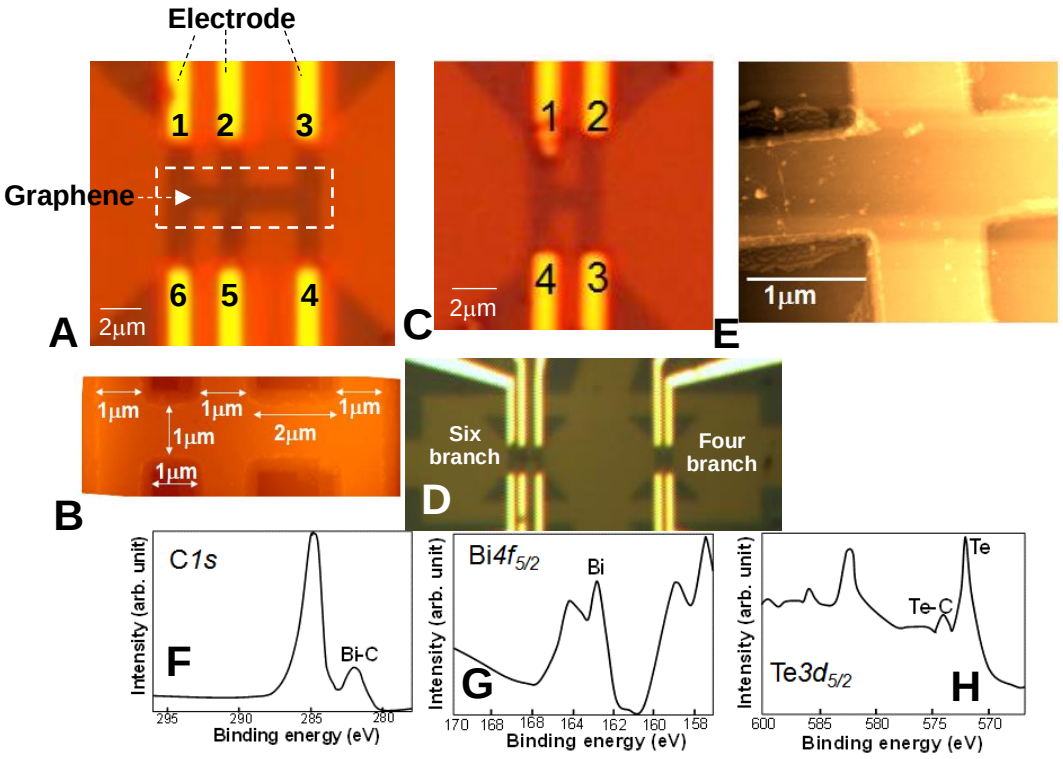

Fig. 1 **(A-C)** Atomic-force-microscope (AFM) images of graphene Hall-bar devices used for resistance measurements of Fig. 2. Panel (B) shows an expansion of the dashed rectangle in (A). For (C), the channel and branch widths are ~1 μm. **(D)** Optical-microscope image of devices in (A) and (C), which are formed at neighboring position on the same segment of CVD-grown graphene (SM1). **(E)** AFM image of graphene decorated with Bi_2Te_3 nanoparticles at $D \sim 4 / 100^2$ nm^2 (~3% coverage ratio); the image is taken at the center of the six branches of (A). **(F-H)** XPS spectra of the samples.

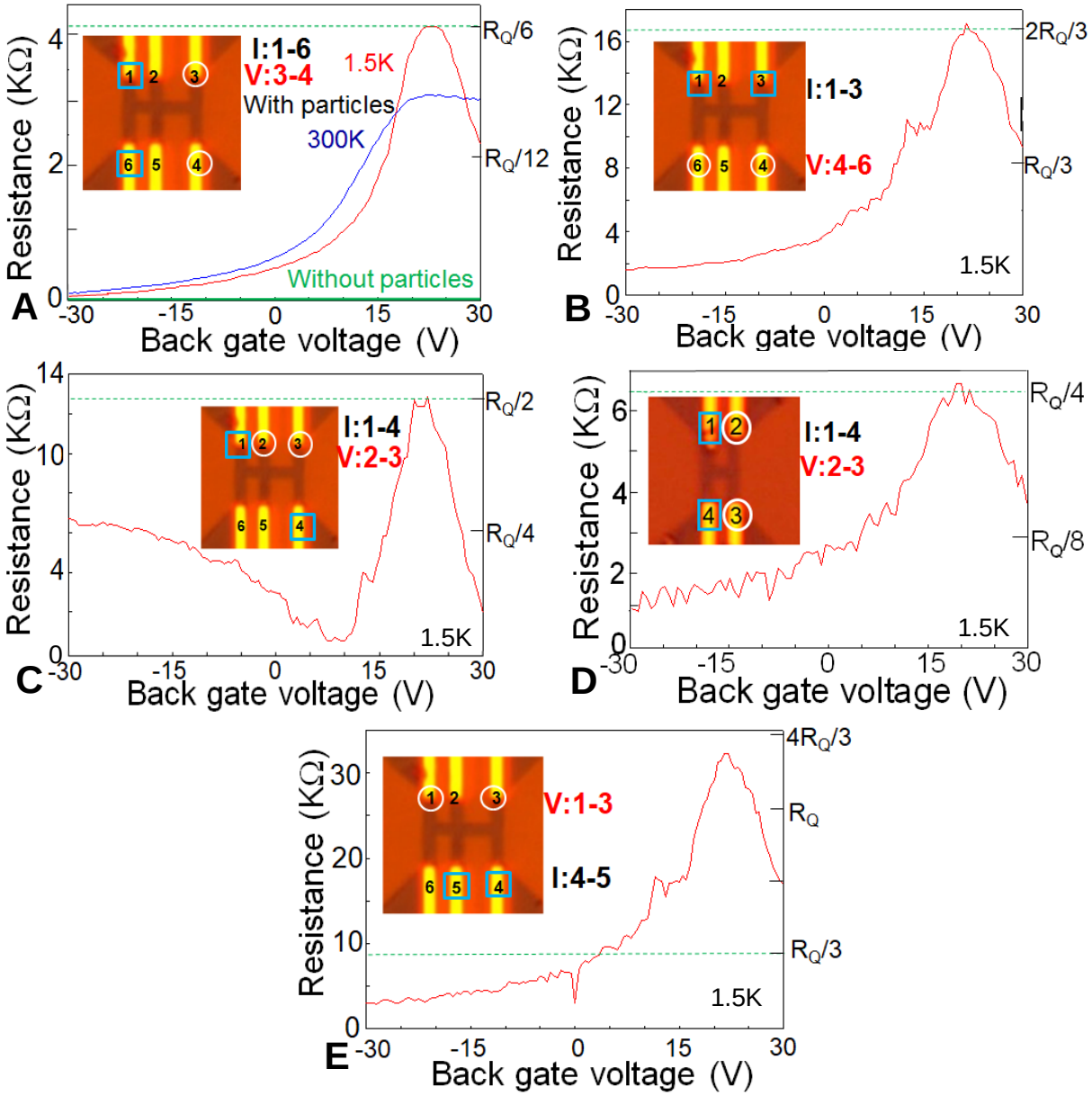

Fig. 2 (A-E) Four-probe resistances versus back-gate voltage (V_{bg}) measured on the samples shown in Figs. 1A through 1D. Current flows between contacts indicated by squares, and voltage is measured across circled contacts; no contact resistances are subtracted. In (A), the green line corresponds to undecorated graphene. All other data corresponds to graphene with nanoparticles at ~3% coverage ratio. The green dashed line in each panel represents quantized resistances predicted for helical edge transport (R_Q is the resistance quantum).

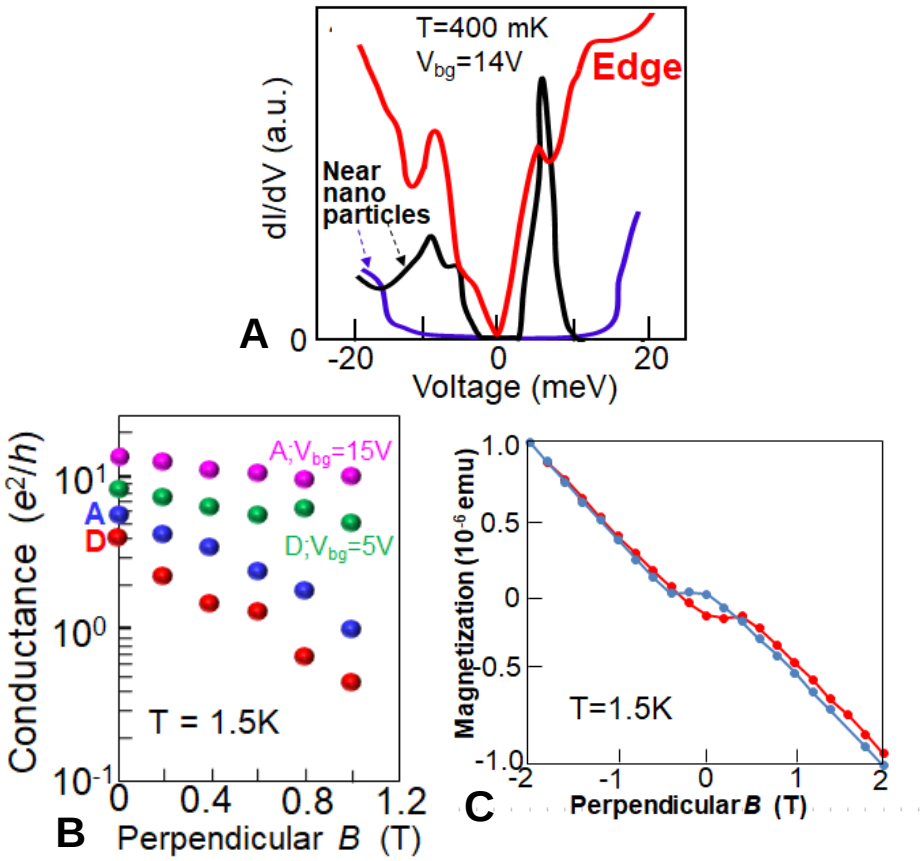

Fig. 3 (A) STS spectra for a sample around V_{bg} for *R* peak, recorded at bulk locations near two different nanoparticles (~50 – 80 nm from particles), showing the maximum (~20 meV; blue line) and minimum (~5 meV; black line) gaps, and at an edge point (~50 nm from edges and ~200 nm away from nanoparticles), revealing the gap disappearance (red line). **(B)** Perpendicular magnetic-field ($B_\perp$) dependence of conductance corresponding to inverse of the *R* peak values of Figs. 2A (blue symbol) and 2D (red symbol) and two off-peak *R* values (pink and green symbols for Figs. 2A and 2D, respectively). **(C)** Magnetization curve of graphene decorated with Bi_2Te_3 nanoparticle in coverage as large as ~10% on $B_\perp$.

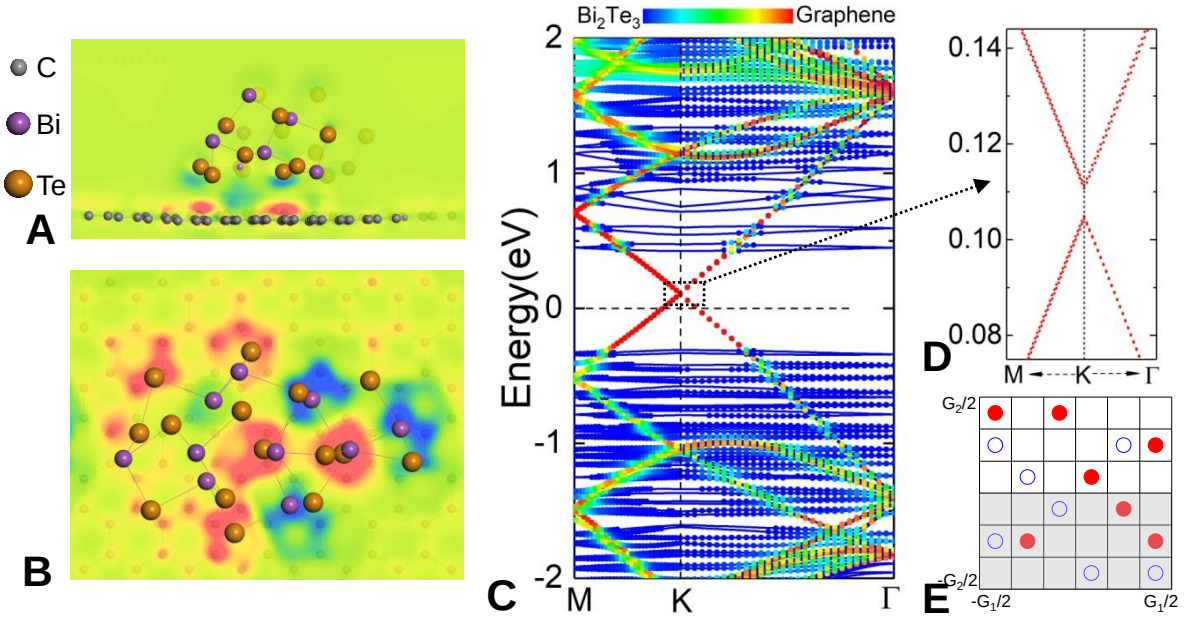

Fig. 4 **(A,B)** Side and top views of the atomic structure and charge-density difference of Bi_2Te_3/Graphene. Red and blue colors respectively indicate charge depletion and accumulation. **(C,D)** Band structure of Bi_2Te_3/Graphene. **(E)** The n-field configuration with red solid, blue hollow circles and blank boxes denoting n= -1, n= 1, and n=0, respectively. Summing the n-fields over half of the torus yields a nontrivial Z_2 invariant.